ELSEVIER

Contents lists available at ScienceDirect

Earth and Planetary Science Letters

www.elsevier.com/locate/epsl



Experimental quantification of permeability of partially molten mantle rock



Kevin J. Miller^{a,*}, Wen-lu Zhu^a, Laurent G.J. Montési^a, Glenn A. Gaetani^b

- ^a Department of Geology, University of Maryland, 314 Regents Dr., College Park, MD 20742, USA
- ^b Department of Geology and Geophysics, Woods Hole Oceanographic Institution, MA 02543, USA

ARTICLE INFO

Article history:
Received 20 May 2013
Received in revised form 23 November 2013
Accepted 1 December 2013
Available online xxxx
Editor: V. Ricard

Keywords:
mid-ocean ridge
partial melt
synchrotron X-ray microtomography
permeability
melt fraction
upper mantle

ABSTRACT

Melt percolation in mantle rocks is currently poorly constrained, especially at low melt fractions. At mid-ocean ridges, for example, geochemical and geophysical observations produce divergent estimates of how much melt is present in the mantle and how quickly it moves. Accurate estimates of permeability and grain-scale melt distribution in mantle rock are necessary to reconcile these observations. We present three-dimensional (3-D), 700 nm-resolution images of olivine-basalt aggregates, containing nominal melt fractions (ϕ_n) between 0.02 and 0.20. Samples were prepared from a powdered mixture of San Carlos olivine and high-alumina basalt and hot-pressed in a solid-medium piston-cylinder apparatus at 1350 °C and 1.5 GPa. Images were obtained using synchrotron X-ray microtomography (SX μ T) from the Advance Photon Source at Argonne National Laboratory. Stokes flow simulations, conducted using the digital melt volume as the numerical domain, determine that the permeabilities of experimental charges range from 2×10^{-16} to 5×10^{-13} m² for $\phi_n = 0.02$ to 0.20, respectively. The simulation results are well represented by the power-law relation between permeability (k) and melt fraction (ϕ), $k = \phi^n d^2/C$, where $n = 2.6 \pm 0.2$, and assuming a grain size of 35 μ m in the experiments, $C = 58^{+36}_{-22}$. These results place important new constraints on rates of melt migration and melt extraction within partially molten regions of the mantle.

© 2013 Elsevier B.V. All rights reserved.

1. Introduction

At mid-ocean ridges, the divergence of lithospheric plates causes an upwelling of hot mantle. The pressure relief during ascent carries peridotite across its solidus and induces partial melting. The melt, which is less dense than the surrounding mantle, separates from the solid and percolates towards the surface via porous and possibly channelized flow (e.g. Kelemen et al., 1997). The melt extraction rate is governed by the permeability of the mantle, which is highly influenced by the amount of melt present as well as the topology and connectivity of the melt network. Despite its importance for understanding melt transport in the mantle, the permeability of partially molten mantle rock is poorly constrained. The aim of this study is to provide better permeability estimates through the quantification of grain-scale melt distribution.

At textural equilibrium, the relationship between permeability and the grain-scale melt distribution in a partially molten rock takes the form of a power law (Cheadle, 1989; Connolly et al.,

2009; McKenzie, 1984; Ricard et al., 2001; von Bargen and Waff, 1986; Wark and Watson, 1998),

$$k = \frac{\phi^n d^2}{C} \tag{1}$$

where d is grain size, n is the power law exponent, and C is a geometric factor influenced by the dihedral angle. For an isotropic system with uniform grain size and shape, n=2 (McKenzie, 2000; von Bargen and Waff, 1986). For more complex systems, where the effects of crystal anisotropy and grain-scale heterogeneity are no longer negligible, higher vales of n should be used. For example, a value of n=3 represents well porous flow through a non-uniform network of packed tetrakaidekahedral grains (Zhu and Hirth, 2003). These model results have been corroborated by permeability experiments conducted on analogue systems composed of quartzite + H₂O and calcite + H₂O where grain size distribution is non-uniform, grain shapes are anisotropic, and $n \sim 3$ (Wark and Watson, 1998).

Mineralogy plays an important role, through its influence on surface free energy, in determining the minimum-energy configuration of the system. Therefore, experiments conducted on partial melts with chemistry similar to the mantle must be considered.

^{*} Corresponding author.

Some permeability experiments (Connolly et al., 2009; Renner et al., 2003) have been conducted for olivine partial melts. They find that the permeability of partially molten olivine basalt at high melt fractions ($\phi > 0.02$) is consistent with a power law where $n \sim 3$. However, permeametry of partially molten aggregates in these experiments is technically challenging. Consequently, the results of such studies are subject to considerable uncertainty.

Grain-scale melt distribution is typically studied by examining backscattered electron images from two-dimensional (2-D) cross-sections of isostatically pressed samples (e.g. Cmíral et al., 1998; Faul and Fitz Gerald, 1999). By assuming a model about the three-dimensional (3-D) connectivity of the melt network, it is possible to infer and estimate sample permeability using the 2-D data. However, those estimates are innately ambiguous, since permeability is an intrinsic property of the 3-D microstructure (Zhu et al., 2011). Therefore, a fully 3-D approach must be employed in order to accurately determine sample permeability. Two methods may be employed for characterizing microstructures in three dimensions: serial cross-sectioning (Garapić et al., 2013; Wark et al., 2003) and synchrotron X-ray microtomography (SXµT) (Watson and Roberts, 2011; Zhu et al., 2011). This study focuses on the latter.

Constraints on mantle permeability come from both geochemical and geophysical observations. Analyses of uranium-series isotopes in mid-ocean ridge basalts (MORB) (Lundstrom et al., 1995; McKenzie, 2000, 1985; Sims et al., 2002; Stracke et al., 2006), have shown a measureable degree of secular disequilibrium between ²³⁸U and its shorter-lived daughter nuclides ²³⁰Th and ²³⁶Ra. Preservation of secular disequilibrium at the surface implies a low melt fraction retained by the mantle, $\phi < 0.01$, with a relatively fast upwelling velocity at $\sim 1~{\rm m\,yr^{-1}}$ (Kelemen et al., 1997). By contrast, geophysical observations imply higher melt fraction. For example, seismic and magnetotelluric data (Evans et al., 1999; The MELT Seismic Team, 1998) from the East Pacific Rise 17°S give evidence that the melt fraction in the mantle is 0.01 to 0.02, implying that melt extraction is inefficient at lower melt fractions. In a more recent study, Key et al. (2013) reported a melt fraction close to 0.10 under the East Pacific Rise 9°N using magnetotelluric inversions. Accurate estimates of permeability of partially molten rocks are needed to reconcile the apparent contradiction in melt fraction.

In this study, we utilize high-resolution SXuT to digitally capture the 3-D melt distributions of olivine-basalt aggregates isostatically pressed in a piston-cylinder apparatus at 1350°C and 1.5 GPa. Nominal melt fractions (ϕ_n) of samples ranged from 0.2 to 0.20 (Zhu et al., 2011). To demonstrate textural equilibrium of these experimental charges, we also conducted time series experiments at nominal melt fraction of 0.05 (refer to the Online Supplement). For each sample, we selected several representative subvolumes and characterized their permeability, grain size distribution, and melt interconnectivity. The permeability of each subvolume was calculated by numerically solving the Stokes fluid questions for the velocity and pressure fields within the digital melt microstructure. Permeability was plotted as a function of the measured melt fraction $(\phi_{\rm m})$ in the corresponding subvolume and an empirical relation between permeability and melt fraction was obtained. Our results provide new experimental constraints on the permeability and melt distribution of partially molten rocks.

2. Experimental methods

2.1. Sample preparation

Experimental charges were prepared from a powder mixture of natural, high-alumina basalt (Mg # = 0.705) and San Carlos olivine (\sim Fo₉₀) (Zhu et al., 2011). Olivine grains were sorted using a sieve

to a maximum grain size of 10 μ m. The nominal melt fraction desired for each sample was obtained by varying the basalt content of the mixture, which was then homogenized with ethanol for six hour-long cycles in an automatic agate mortar and pestle. The homogenized mixtures were pressed into cylindrical pellets under a 1-ton press, placed into graphite capsules (Fig. 1A), and dried overnight at 400 °C to remove water. The whole assembly was centered in a straight-walled graphite furnace using crushable MgO spacers. The pressure medium for all experiments consisted of a CaF₂ sleeve.

Experiments were conducted using 1.27 cm assemblies (Boyd and England, 1960). Pressure was initially applied using the cold piston-in technique (Johannes et al., 1971). The friction correction for the assemblies was calibrated against the Ca-tschermakite breakdown reaction at 1.2 to 1.4 GPa and 1300 °C (Hays, 1966) and determined to be less than the pressure uncertainty, so no correction has been applied to the reported pressures. Temperature was measured and controlled using a W₃Re₉₇/W₂₅Re₇₅ thermocouple; no correction for the effect of pressure on thermocouple EMF has been applied to the reported temperatures. N2 was flowed over the thermocouple wires to minimize thermocouple oxidation over the course of an experiment. Temperatures are estimated to be accurate to $\pm 10\,^{\circ}$ C and pressures to ± 50 MPa. The temperature difference over the capsule was determined to be less than 5°C using offset thermocouples. Experiments were terminated by shutting off the power. Upon completing each experimental run, the graphite capsule was sawed open to expose the surface of the experimental charge (Fig. 1B). The exposed surface was polished and reflected light photomicrographs were taken. A cylindrical ~0.9 mm diameter samples was then cored from each charge to be used for SXµT analysis (Fig. 1C).

Two suites of experiments were conducted (Table 1). The first suite was a time series, which was conducted to determine the minimum time required for a sample to reach textural equilibrium. All of the time series samples have a nominal melt fraction of 0.05 and the sintering time varied systematically from 42 to 336 hours (see Online Supplement). The second suite of samples consisted of nominal melt fractions of 0.02, 0.05, 0.10, and 0.20. The sintering time for each sample was sufficiently long to ensure textural equilibrium (Zhu et al., 2011).

3. Analytical methods

3.1. Synchrotron X-ray microtomography

Microtomography was conducted at 2-BM of the Advanced Photon Source at Argonne National Laboratory, Argonne, IL. A multilayer monochromator was used to select a narrow band (27 keV) of X-rays. Those photons were then passed through the olivine-basalt sample (Fig. 2). On the opposite side of the sample, the X-rays were transmitted to a LuAg:Ce scintillator, converting them into visible light. A CCD camera was used to detect the visible light, and the light intensity was recorded. The sample was rotated 180° in 0.12° increments to build a digital volumetric representation of the sample in about 20 min (Fig. 2). For each sample, the raw intensity data was processed using GRIREC (Dowd et al., 1999) into a stack of image slices. Each slice is a grayscale image whose constituent pixels have values that are functions of X-ray attenuation, which is in turn, a function of material density. In this way, SXµT is used to differentiate phases, so long as the density contrast between the phases is substantial.

Silicate melt samples pose a unique problem in that the density contrast between olivine and basalt is not sufficient to differentiate the phases using standard phase contrast techniques. To circumvent this issue, we employed diffraction-enhanced imaging (Fitzgerald, 2000) to improve the contrast between olivine

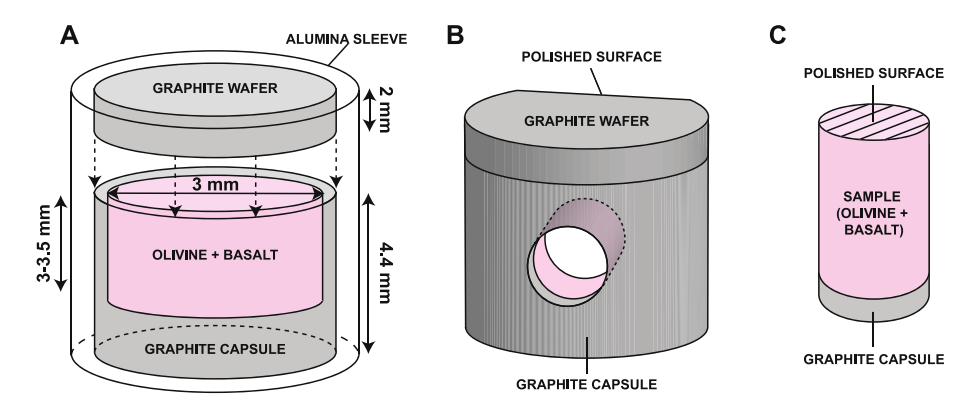


Fig. 1. Schematic diagram of experimental setup before and after sintering. (A) Starting materials before sintering. The graphite capsule (gray), which is packed with the powdered olivine/basalt mixture (pink), is placed in an alumina sleeve with a graphite wafer as a lid. (B) Sample assembly after sintering. One side of the sample assembly is cut and the surface of the sintered aggregate is polished. The hole in the sample assembly illustrates where the sample (C) is taken for X-ray imaging. Hash marks represent the polished surface. (For interpretation of the references to color in this figure legend, the reader is referred to the web version of this article.)

Table 1 Summary of experiments.

Sample ID	Nominal melt fraction, $\phi_{ m n}$	Sintering time [h]	Measured melt fraction $^{\mathrm{a}}$, ϕ_{m}	Grain size ^b , d [μm]	Permeability ^c , <i>k</i> [m ²]
scoba-5	0.20	265	0.18 ± 0.02	40(-17/+28)	$2.3(-0.4/+0.4) \times 10^{-13}$
scoba-6	0.10	240	0.079 ± 0.009	37(-14/+22)	$1.9(-0.5/+0.6) \times 10^{-14}$
scoba-9	0.02	336	0.015 ± 0.003	42(-20/+39)	$4.1(-0.7/+0.8) \times 10^{-16}$
scoba-12 ^d	0.05	168	0.048 ± 0.004	32(-12/+18)	$5.2(-1.1/+1.3) \times 10^{-15}$
scoba-13 ^d	0.05	42	N/A	N/A	N/A
scoba-14 ^d	0.05	84	N/A	N/A	N/A
scoba-15 ^{d,e}	0.05	336	0.0570	29.6	7.7×10^{-15}

- a $\phi_{
 m m}$ are arithmetic average measured melt fractions and 1σ standard deviations computed over range of subvolumes per sample.
- $^{
 m b}$ d are geometric average equivalent diameters with 1σ standard deviations computed for EDD of the aggregated subvolumes.
- $^{\rm c}$ k are geometric average permeabilities with 1σ geometric standard deviations computed over range of subvolumes per sample.
- d Time series experiments: no physical properties calculated on samples that have not yet achieved textural equilibrium.
- ^e The values for scoba-15 were calculated from only one $350 \times 350 \times 350 \,\mu\text{m}^3$ subvolume.

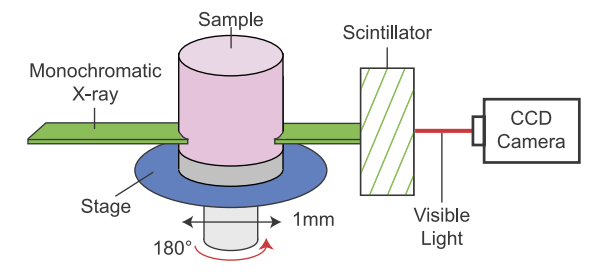


Fig. 2. Schematic diagram of the imaging process. A monochromatic X-ray (green) is transmitted through the sample onto a scintillator (dashed-green), where it is converted to visible light (red), and recorded by a CCD camera. During a microtomography experiment, the sample is rotated 180° to create a series of cross-sectional data used to construct the 3-D digital image. (For interpretation of the references to color in this figure legend, the reader is referred to the web version of this article.)

and basalt (Zhu et al., 2011). Diffraction-enhanced imaging utilizes the interference pattern, which occurs in the near-field Fresnel diffraction regime, to highlight the olivine-basalt interfaces and produce high-resolution 3-D microstructure of olivine-basalt systems.

3.2. Subvolume selection

In order to increase efficiency of computation, we selected only a few cubic subvolumes per sample for analysis. The size of those subvolumes ranged from $140\times140\times140~\mu m^3$ (i.e. $100\times100\times100~pixel^3)$ to $350\times350\times350~\mu m^3$ (i.e. the $500\times500\times500~pixel^3)$ (Fig. 3). We determined through a series of permeability analyses on progressively larger subvolumes that a $350\times350\times350~\mu m^3$ subvolume is sufficiently representative of the sample microstructure. Refer to Online Supplement for details.

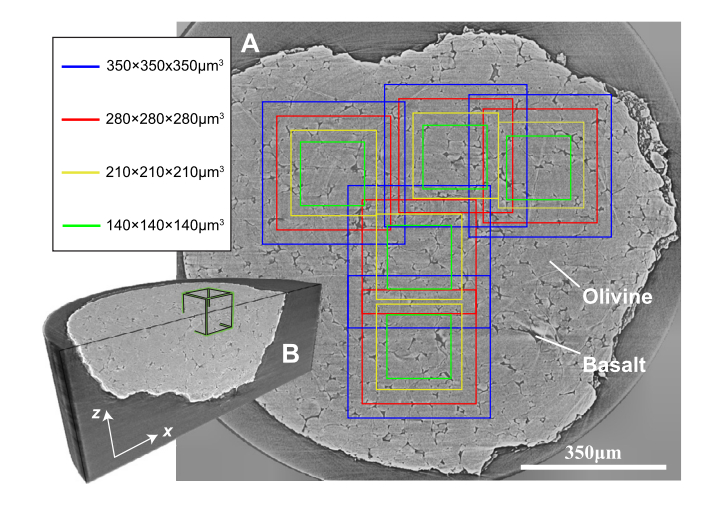


Fig. 3. Subvolumes sampling. (A) Tomography slice from the middle of scoba-12 ($\phi_n = 0.05$). Subvolumes of various sizes, shown as colored boxes, are defined from (B) the larger 3-D reconstructed image. The permeability of each subvolume was calculated in order to quantify the variation in microstructure within each sample and to determine the minimum size for a representative volume (see Fig. S3).

Several $350 \times 350 \times 350~\mu m^3$ subvolumes from each sample were analyzed. Although each subvolume is susceptible to local heterogeneities in the melt microstructure, taken together, these subvolumes adequately represent the melt microstructure of the entire sample. Analyses of sample permeability, grain size, and interconnectivity were conducted using a combination of Avizo® and Matlab® software.

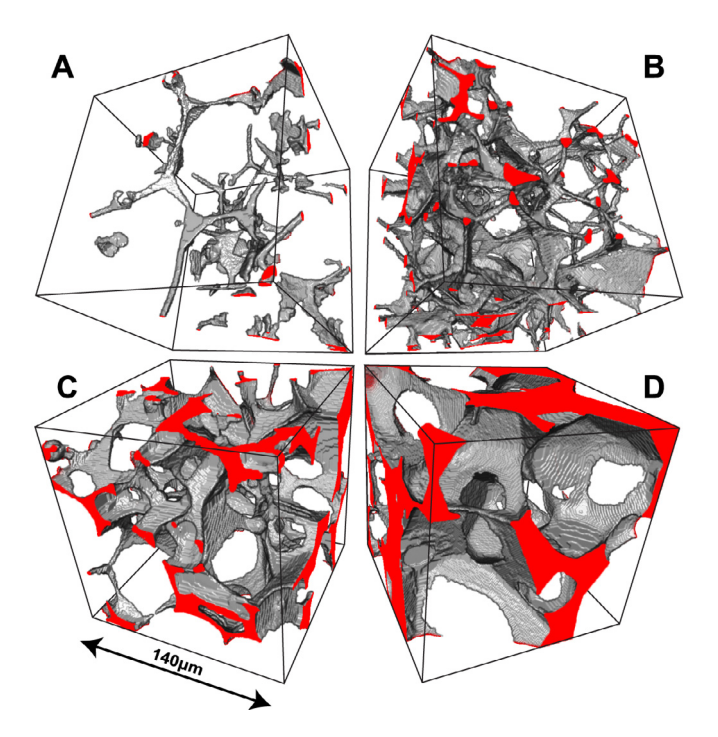


Fig. 4. Volume renderings of the melt distribution for olivine–basalt containing nominal melt fractions of (A) 0.02, (B) 0.05, (C) 0.10, and (D) 0.20. The dimensions of each subvolume are $140 \times 140 \times 140 \text{ µm}^3$. Gray represents the melt phase, empty spaces are olivine grains, and red highlights the intersection of melt and the bounding box. (For interpretation of the references to color in this figure legend, the reader is referred to the web version of this article.)

3.3. Noise reduction and segmentation techniques

To reduce noise and suppress artifacts that remain from the imaging process, we employed a non-local means filter (Buades et al., 2005) and an anisotropic diffusion filter (Weickert et al., 1998) (Fig. S1). Once we reduced the noise to an acceptable level, we implemented a series of algorithms to segment the grayscale data. Segmentation is a procedure by which we transform grayscale data into a binary label file required for our quantitative analyses of the microstructure (Fig. S2). Two techniques were used for segmenting the grayscale data: a marker-based watershed transformation and a top-hat threshold.

The watershed transformation (Beucher, 1992) is based on the idea of redefining grayscale pixel value as topographic relief. First, interphase boundaries are highlighted by thresholding the grayscale gradient of the denoised image. Then a global threshold is employed to make an initial try at segmenting the denoised data. The image is then inundated starting from the initial segmentation. The regions defined by the thresholded gradient act as impermeable barriers to the rising virtual fluid, preventing the merging of distinctly different phases. The result, after the watershed transformation, is a high-quality, segmented binary image where phase boundaries are defined exactly at grayscale inflections

The watershed transform is suitable for accurately segmenting larger features in the data; however, it tends to miss very thin melt conduits. To capture these finer details, a top-hat filter (Vincent, 1993) is applied and then a global threshold is utilized to select those details. The kernel width is selected based on the size of those features. An opening filter is then applied to the inverse of the image in order to smooth out the boundaries of the image. Some user-controlled refinements of the binary image were typically needed. The size of the features that top-hat segmenting is able to recognize is limited by the kernel size. Avizo limits the kernel width to twenty pixels, so a watershed transform is still

needed if there are features in the 2-D slice that are larger than the kernel size. Examples of the final 3-D binary images for four charges of different nominal melt fractions are show in Fig. 4.

3.4. Quantification of network topology

We performed a series of systematic analyses on subvolumes of the 3-D binary image of our olivine–basalt samples. We quantify the melt fraction, grain size distribution, network interconnectivity, and permeability for each subvolume (Table S1).

The melt fraction (ϕ_m) of each subvolume is measured by calculating fraction of voxels, the three-dimensional image unit, assigned to the melt phase in the segmented image. The measured melt fraction of a subvolume may vary from the nominal melt fraction (ϕ_n) because of sample heterogeneity and possible melt-rock interactions. Uncertainty on the measured melt fraction was estimated by contracting (low bound) and dilating (upper bound) the binary melt image by one pixel (Fusseis et al., 2012). For this reason, error bars are asymmetric.

Grain size distribution was quantified using Avizo's Separate Objects module. The module takes the binary label image as input and performs a series of high-level algorithms, including a watershed transform, distance transform, and logical operations, to separate individual grains by a 1-pixel boundary. We report the grain size distribution for every subvolume as the distribution of equivalent diameters. Separation of individual grains is difficult when melt fraction is low, since the only thing that separates grains are melt channels. Therefore large uncertainties in the equivalent diameter distributions are expected for the scoba-9 ($\phi_n = 0.02$) sample.

Quantification of the melt network connectivity was accomplished using Avizo's skeletonization module. Skeletonization is the process by which the general melt microstructure is simplified to an interconnected skeleton network. The skeleton is used to assess the topology of the melt network. First, a distance map is calculated. Second, a thinning algorithm is applied to the binary image that removes pixel-by-pixel the outer layers of melt channels until only a string of pixels remain. The algorithm is calibrated so as to preserve small features of the melt microstructure. Finally, the mean thicknesses of the melt conduits are retrieved from the distance map. A Matlab® script, called *ScobaCleaner.m*, was written to automatically remove spurious features from the skeletonized melt network (see supplementary material and Zhu et al., 2011).

3.5. Quantification of permeability

Permeability calculations were performed using Avizo's XLab Hydro module. Two different computational modules were used: the Absolute Permeability Experiment Simulation (APES), which computes a scalar estimate of the permeability, and the Absolute Permeability Tensor Calculation (APTC), which computes the 3×3 permeability tensor for the subvolume. Both APES and APTC implement the finite volume method (Harlow and Welch, 1965) to solve the Stokes Equations for the velocity and pressure fields. The Stokes Equations are given by

$$\begin{cases} \nabla \cdot \mathbf{u} = 0 \\ \mu \nabla^2 \mathbf{u} - \nabla p = \mathbf{0} \end{cases}$$
 (2)

where p is the pressure [Pa], μ is the viscosity [Pas] of the simulated fluid, and ${\bf u}$ is the velocity [ms⁻¹].

For APES, flow in the digital melt domain is driven by a pressure differential (ΔP) imposed across the subvolume (Fig. 5). A 1-pixel-wide impermeable layer is added to the sides of the sample domain parallel to the flow in order to prevent loss of fluid through the adjacent faces. Accommodation zones are added to the inflow and outflow faces of the subvolume to ensure that there is a self-consistent pressure field over the faces. The APES module then

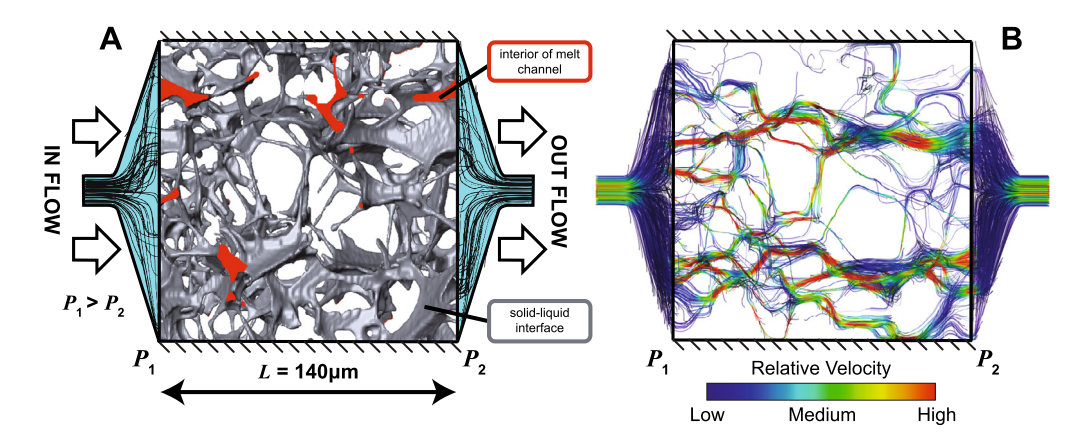


Fig. 5. (A) Schematic diagram of a virtual permeability experiment conducted using APES module along the *z*-axis of a $140 \times 140 \times 140$

solves for the velocity field in the melt domain (Fig. 5). Each APES fluid flow simulation was conducted along the *z*-direction, parallel to the cylindrical sample axis. During post-processing, the volumetric flux Q [m^3 s⁻¹] across the sample end faces is computed, and an application of Darcy's Law yields the permeability k [m^2]

$$k = -Q \frac{\mu}{\Delta P} \frac{L}{A} \tag{3}$$

where A is the cross-sectional area $[m^2]$ and L [m] is the length of the computational domain.

Contrary to the APES, APTC simulates fluid flow by solving a modified, non-dimentional, volume-averaged form of the Stokes Equations (Gray, 1975)

$$\begin{cases} \nabla \cdot \mathbf{D} = \mathbf{0} \\ \nabla^2 \mathbf{D} - \nabla \mathbf{d} = \mathbf{I} \end{cases}$$
 (4)

where \mathbf{D} is a tensorial representation of the spatial deviation of the velocity, \mathbf{d} is a vectorial representation of the spatial deviation of the pressure, and \mathbf{I} is the 3×3 identity matrix. Rather than invoking Darcy's Law, the non-dimensional effective permeability tensor \mathbf{K} is computed by volume-averaging \mathbf{D} over the whole computational domain V.

$$\mathbf{K} = \frac{1}{V} \int_{V} \mathbf{D} \, dV \tag{5}$$

Equation systems (2) and (4) do not lend themselves immediately to solving through implicit methods, since matrices of this form are singular. Therefore, an artificial compressibility coefficient (Chorin, 1967) is incorporated in the discretized forms of Eq. (2) and (4).

Differing from the APES module, which imposes a pressure gradient to induce fluid flow, the APTC module supplies mass to the system via a volumetric source term in the discretized formulation of Eq. (4). Accommodation zones are defined on all six faces of the subvolume to impose periodic boundary conditions between parallel faces. One major drawback of the APTC module is computational cost of the calculation. Moreover, significant permeability anisotropy is not expected in our isostatically pressed samples. The APES module, in contrast, is a relatively quick computation capable of calculating the scalar permeability for a given subvolume, provided the permeability is not significantly anisotropic. For our study, APES is the preferred module for calculating sample permeability. APTC is only used to verify the absence of significant permeability anisotropy.

4. Results

The analyses mentioned above were performed on all $350 \times 350 \times 350 \ \mu m^3$ subvolumes for nominal melt fractions ranging from 0.02 to 0.20. Refer to Table S1 of the online supplement for a complete list of results. From now on, subvolumes will be referred to using the notation "scoba-*a-b-c*", where the placeholders *a*, *b*, and *c* refer to the sample number, subvolume dimension in pixels, and the subvolume identification number, respectively (Table S1).

4.1. Grain size results

Results from our time series experiments (Online Supplement) indicate that the olivine-basalt samples with $\phi_{\rm n}$ of 0.02, 0.05, 0.10, and 0.20 have equilibrium textures.

The olivine–basalt aggregates with ϕ_n from 0.05 to 0.2 exhibit lognormal Equivalent Diameter Distributions (EDD). However, the scoba-9 sample ($\phi_n=0.02$) has an EDD that differs significantly from the others, which likely results from a failure of the *Separate Objects* module to accurately segment individual grains at small melt fractions. For melt fractions as low as 0.02, many of the melt channels are below the resolution of SX μ T (Zhu et al., 2011). When this is the case, two or more adjacent grains may be misrepresented as a single large grain. This may explain why the mean EDD reported for scoba-9 is much larger than the others, and it may also explain why the EDD exhibits a long tail for equivalent diameters larger than 80 μ m. These larger grains cannot be remnants of the pre-sintered samples, since the maximum grain size of the pre-sintered experimental charge is 10 μ m.

The mean equivalent diameters for scoba-9 ($\phi_n=0.02$), scoba-12 ($\phi_n=0.05$), scoba-6 ($\phi_n=0.10$), and scoba-5 ($\phi_n=0.20$) are 42^{+38}_{-20} µm, 34^{+18}_{-12} µm, 38^{+21}_{-13} µm, and 41^{+24}_{-15} µm, respectively (Fig. 6). Errors are asymmetric because equivalent diameter distributions are characteristically lognormal.

4.2. Connectivity of melt network

Results from connectivity analyses are conveyed as Coordination Number Distributions (CND) in Fig. 7. The skeletonization analysis replaces melt-filled triple junctions with tubules whose widths vary along their axes. The intersections between melt tubules are designated "nodes." Connectivity is defined as the number of melt tubules connected to each node. The connectivity of an ideal melt network is predicted to be 4 (von Bargen and Waff, 1986), but it varies in natural systems like our samples (Zhu et al., 2011). We determine the CND of one $350\times350\times350$ μm^3 subvolume from each sample.

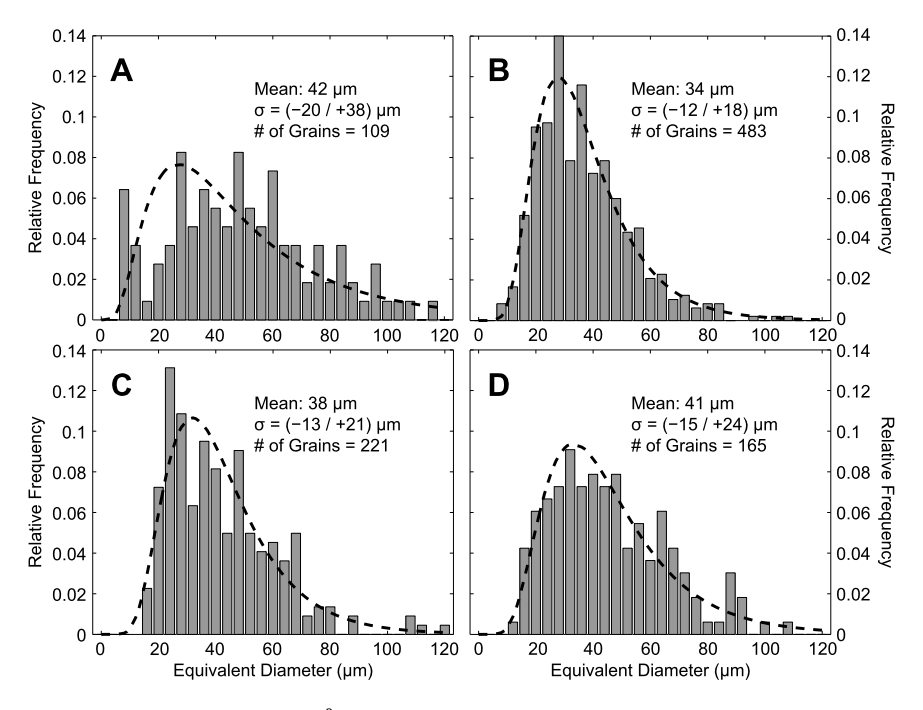


Fig. 6. Equivalent diameter distributions from $350 \times 350 \times 35$

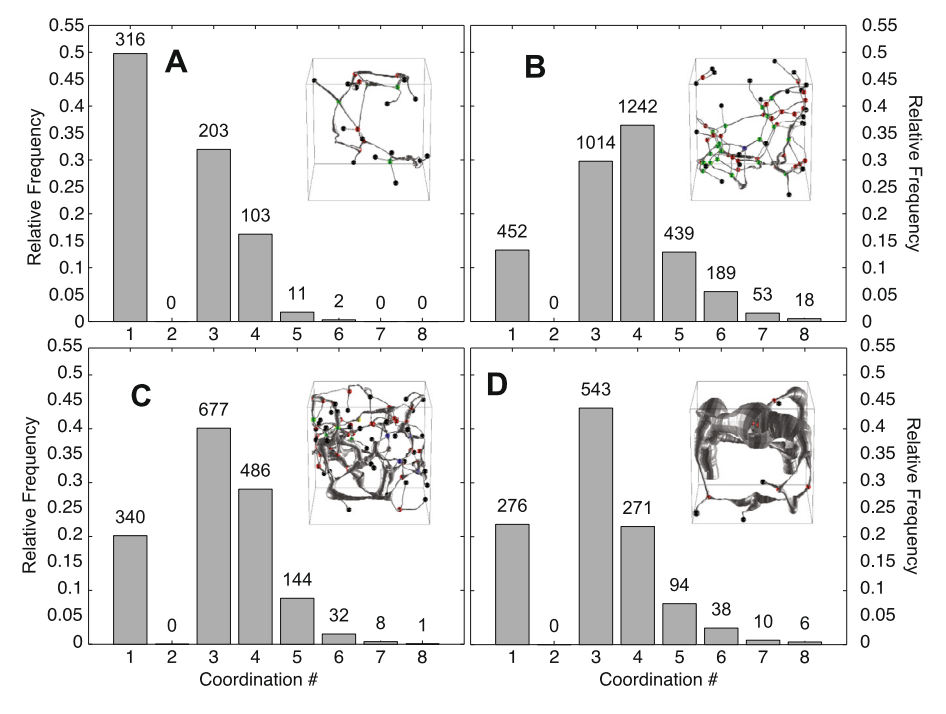


Fig. 7. Coordination number distribution of melt fraction series experiments. Relative frequency of coordination numbers of $350 \times 350 \times 350$

To describe the CND in a physical context, nodes with a coordination number of 1 represent dead-end melt channels. Nodes with a coordination number of 2 are removed from the skeleton, since two connected melt conduits effectively act as one single conduit. Nodes with a coordination number of 3 are mostly associated with regions where melt pooling or grain boundary wetting is occurring. A node with a coordination number of 4 indicates a four-grain

junction. Nodes with a coordination number of 5 or higher are either representative of physical junctions in which more than four grains are present, or artifacts from the *ScobaCleaner.m* algorithm when the connections from short tubules get merged (Table S2).

The CNDs of scoba-5 ($\phi_n=0.20$), scoba-6 ($\phi_n=0.10$), scoba-12 ($\phi_n=0.05$), and scoba-9 ($\phi_n=0.02$) indicate that the frequency of coordination number 4 nodes decreases as melt fraction increases

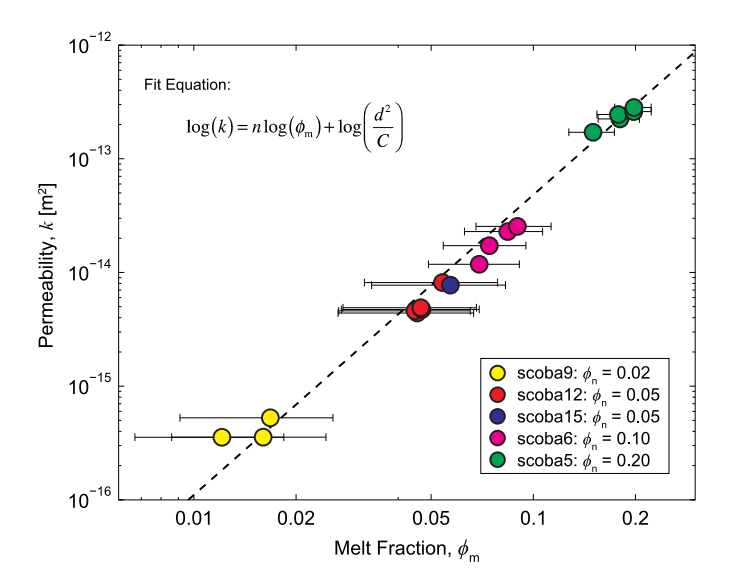


Fig. 8. Permeability calculated for $350 \times 350 \times 350 \ \mu m^3$ subvolumes plotted as a function of the measured melt fraction on log-log axes. Different samples are represented by different colors, with sample number and nominal melt content indicated in the legend. The dashed line represents the best-fit line for $\log_{10}(k) = \log_{10}(\phi_{\rm m}) + \log_{10}(d^2/C)$, where geometric constant $C = 58^{+36}_{-22}$ and power law exponent $n = 2.6 \pm 0.2$. For fit, d is assumed to be 35 μ m, a value we chose because it is within the range of grain sizes measured from all subvolumes.

(Fig. 7). This represents a decrease in the number of melt junctions connected to four melt tubules. Conversely, the frequency of coordination number 3 increases over the same range, representing an increase in melt grain boundary wetting. The higher connectivity nodes, e.g. 5–8, have more or less the same frequency across scoba-12, scoba-6, and scoba-5.

Scoba-9 ($\phi_{\rm n}=0.02$) appears to contradict the progression towards a coordination number 4 dominated melt microstructure, since coordination number 3 nodes represent a clear majority of the nodes in the network. However, many thin melt tubules in scoba-9 appear broken and register as nodes having a connectivity of 1. This artifact is a result of the SXµT resolution limits. A node having four connected tubules might register as a node that has only three connecting tubules if one of those tubules is removed during cleaning or data processing. This would account for the anomalously high abundance of dead-end tubules as well as the less-than-expected frequency of coordination number 4 nodes. Notwithstanding these resolution limits, it is clear that the melt network remains well connected even when the nominal melt fraction is 0.02 and the measured melt fraction of representative subvolumes approaches $0.0121^{+0.006}_{-0.005}$. Therefore, even at low melt fractions, our subvolumes support fluid flow.

4.3. Permeability results

Permeability was computed for three to five $350 \times 350 \times 350 \ \mu m^3$ subvolumes per sample (Fig. 3). Fig. 8 shows the calculated permeability as a function of the measured melt fraction of each subvolume. We performed a linear fit on the data using the total least squares algorithm based on York et al. (2004), including the standard error on measured melt fraction. Since permeability values were calculation results, no uncertainty was reported. Uncertainty of melt fractions came from the ambiguity in the location of the olivine–basalt phase interface. The upper and lower bounds of melt fractions were estimated by expanding and shrinking the melt phase by 1 pixel at the olivine–melt interface (Fusseis et al., 2012). When fitting the data, we shift the porosity value to halfway between the upper and lower bounds of melt fraction. We find that fluid flow in our olivine–basalt samples is well characterized

by a power-law relationship between permeability and melt fraction (Eq. (1)), where the power law exponent is $n=2.6\pm0.2(1\sigma)$, and, assuming a grain size of 35 μ m in our samples, the geometric constant is $C=58^{+36}_{-22}(1\sigma)$.

4.4. Permeability anisotropy

We computed the permeability tensor **K** for the scoba-12-500-4 subvolume ($\phi_n = 0.05$) using the APTC module, yielding

$$\mathbf{K} = \begin{bmatrix} 1.86 & 2 \times 10^{-3} & -6 \times 10^{-2} \\ 2 \times 10^{-3} & 1.90 & 8 \times 10^{-2} \\ -6 \times 10^{-2} & 8 \times 10^{-2} & 1.94 \end{bmatrix} \times 10^{-15} \,\mathrm{m}^2 \tag{6}$$

The eigenvalues of **K**, called the principal permeabilities, are $2.02\times 10^{-15}~\text{m}^2,~1.88\times 10^{-15}~\text{m}^2,~\text{and}~1.81\times 10^{-15}~\text{m}^2.$ The relative variance of these values is $\sim\!0.6\%$, which is negligible compared to modeling uncertainty. The off-diagonal terms of **K** are also $\sim\!20$ to 1000 times smaller than the diagonal terms. Therefore, we conclude that the melt microstructure of our sample is isotropic at the scale of this $350\times 350\times 350~\text{µm}^3$ subvolume. Since the microstructures are isotropic, we conclude that isostatically pressing the samples produces an isotropic permeability structure, so the APES module is sufficient for computing the permeabilities of our subvolumes.

The permeability of this subvolume, as determined using APES, is 4.6×10^{-15} m², which is about a factor of 2 larger than the determination from APTC. The discrepancy is likely due to the different formulation of the permeability determination problem. The formulation used by APES is closest to the original definition of permeability and is therefore preferred here. We also artificially rotated the subvolume and recalculated the permeability by APES in three mutually perpendicular directions. We find the permeabilities to be 5.4×10^{-15} m², 4.7×10^{-15} m², and 4.6×10^{-15} m² for k_x , k_y , and k_z , respectively. Permeability values are similar within $\sim 3.9\%$ relative variance, which confirms that the permeability in our samples is essentially isotropic.

5. Discussion

5.1. Morphology of melt microstructure

Visual inspection of our melt microstructures reveals that, for low melt fractions, the network topology resembles the ideal model proposed by von Bargen and Waff (1986), where melt preferentially reside to three and four-grain junctions. As the nominal melt fraction increases to 0.05, we visually observe the onset of grain boundary wetting, though melt tubules continue to be the dominant feature of the melt microstructure. At $\phi_n = 0.10$, there is an inversion from a tube-dominated network to one in which the melt films and pools are the most prominent features. Finally, for $\phi_n = 0.20$, grain boundaries are almost completely wetted, as the sample is approaching its theoretical disaggregation limit, $\phi_n \geqslant 0.20$ (Hier-Majumder et al., 2006; McKenzie, 1984).

5.2. Interpretation of power law exponent

The permeability of an ideal melt network, in which grain size is uniform, depends on the square of melt fraction, i.e., n=2 when melt resides at triple junction (von Bargen and Waff, 1986) and on the cube of melt fraction, i.e. n=3, as higher melt fraction (Wark et al., 2003). This transition may correspond to the two morphological regimes observed here, i.e. a tubule-dominated at low melt fractions (n=2) versus pool and film-dominated at higher melt fractions (n=3). Considerations of grain-scale heterogeneity would also produce n=3 (Zhu and Hirth, 2003). However, the data from this study are captured adequately by a single relation with

 $n=2.6\pm0.2$ and $C=58^{+36}_{-22}$. More complex relations are not justified by the data, considering the uncertainty of our porosity and permeability estimates.

The experimental results of Renner et al. (2003) and Connolly et al. (2009) are compatible with n = 3, which, considering that these experiments infer permeability indirectly from the compaction rate of olivine-basalts aggregate, present an encouraging agreement with our study. Therefore, microstructure readjustment during quenching appears to be minor in our experiments and our permeability-porosity relation can probably be used to describe olivine-basalt aggregates at mantle conditions. For extrapolation to higher temperatures and pressures, we may need to consider an increased importance of melt film grain faces, as the dihedral angle appears to decrease as temperature and pressure increase (Yoshino et al., 2009). However, melt films observed at high melt fraction in our sample do not have a marked effect on our permeabilityporosity relation. Future work would need to address their contribution to permeability at low melt fraction, high pressure, and high temperature.

Given the various melt geometries present in our datasets, a value of n=2.6, between 2 and 3, is not surprising. Consider a mixture of subvolumes consisting of end member melt distributions, one end member is entirely made up of melt tubules along triple junctions (n=2) while the other contains only wet grain boundaries and melt pools (n=3). The overall permeability of the system is the mixing of the individual subvolume permeabilities and, in the absence of a large-scale order between these subvolumes, will converge to the geometric mean permeability as the number of subvolumes increases (Madden, 1976). If the permeability of each subvolume V_i is given by the empirical relation $k_i = C_i \phi^{n_i}$, the geometric mixing leads to an equation for the total permeability k_T

$$k_{\rm T} = (C_1 \cdots C_N)^{\frac{1}{N}} \phi^{\frac{n_1 + \cdots + n_{\rm N}}{N}}$$
 (7)

where N is the total number of subvolumes. Eq. (7) is, in its own right, a power law, the same as Eq. (1). In our case, the end member distributions have n=2 and n=3, so Eq. (7) leads to a new power law exponent of 2.5, which is consistent with the value of $n=2.6\pm0.2$ obtained by our fit. A value of $n=2.6\pm0.2$ between 2 and 3 can be thought of as representing a mixing of melt geometries.

5.3. 1-D mantle model

Given the new empirical relation between permeability and the melt fraction, we make a simple model of melt transport in the mantle. If 230 Th disequilibrium observed is produced at 60 to 75 km depths, melt transport must have occurred at a velocity w of order of 1 m yr⁻¹ (3 × 10⁻⁸ m s⁻¹). Darcy's law implies

$$\phi w = \frac{k_0}{\mu} \phi^n \Delta \rho g \tag{8}$$

where $k_0=d^2/C$ is the permeability coefficient, ϕ is the porosity, $\Delta \rho$ is the density contrast between melt and solid mantle, $\mu=10$ Pas is the melt viscosity (Ryan and Blevins, 1987) and $g\sim 10~{\rm m\,s^{-1}}$ is the acceleration of gravity.

Assuming a grain size of 3 mm (Toramaru and Fujii, 1986), we estimate $k_0 \sim 1.55 \times 10^{-7}$ m². If $\rho_s = 3300$ kg m⁻³, $\rho_f = 2700$ kg m⁻³ (Stolper et al., 1981), $\Delta \rho = 600$ kg m⁻³. From Eq. (8), the porosity needed to sustain a melt velocity w is given by

$$\phi = (W/\beta)^{\frac{1}{n-1}} \tag{9}$$

where $\beta=k_0\Delta\rho g/\mu=9.3\times 10^{-5}~m\,s^{-1}$. Therefore, preserving ²³⁰Th disequilibrium produced at depth requires a porosity of at least 0.0068. This number is comparable with estimates from seismic studies (The MELT Seismic Team, 1998), although at the low

end of the observational constraints. Higher porosity results in faster melt velocity, which is more easily reconciled with ²³⁰Th excess in mid-ocean ridge basalts.

An alternative estimate of mantle porosity can be obtained from a mass balance between melt produced by decompression of a mantle column at velocity W (Ribe, 1985; Spiegelman and Elliott, 1993):

$$\rho_{\rm f}\phi w = \rho_{\rm s} F W \tag{10}$$

where F is degree of melting, which increases with height above the level where melt starts. By combining Eqs. (8) and (10), the mean melt fraction retained by our model mantle is estimated at.

$$\phi = \left(\frac{\rho_{\rm s}}{\rho_{\rm f}} \frac{FW}{\beta}\right)^{\frac{1}{n}} \tag{11}$$

Remarkably, the permeability in this model does not depend on porosity but only on geodynamical parameters

$$k = \frac{\rho_{\rm S}}{\rho_{\rm f}} \frac{\mu FW}{\Delta \rho g} \tag{12}$$

Assuming F=0.20 at the top of the melting column (Asimow et al., 1995) $W=5~{\rm cm\,yr^{-1}}~(1.7\times10^{-9}~{\rm m\,s^{-1}})$ (Spiegelman and Elliott, 1993), we obtain a melt fraction $\phi=0.0085$, and according to Eq. (8), a melt velocity of $5.0\times10^{-8}~{\rm m\,s^{-1}}~(\sim1.6~{\rm m\,yr^{-1}})$.

If this velocity is valid for the entire melting column, the transit time through the melting column z_M would be

$$t_{U} = \frac{z_{M}}{w} = \left(\frac{\rho_{S}}{\rho_{f}} F_{M} W\right)^{\frac{1-n}{n}} \beta^{-1/n} z_{M}$$
 (13)

where F_M is the degree of melting in the column. However, the degree of melting increases upward in the column. Assuming a linear increase of F from 0 to F_M through a column of height z_M , we obtain

$$t_T = nt_U \tag{14}$$

For $F_M=0.2$ and $z_M=75$ km, $t_T\sim 136$ kyrs. This value is in the high end of what is permissible to preserve 230 Th excesses, especially considering that chromatographic effect will reduce the velocity of isotopes (Spiegelman and Elliott, 1993). However, the transit time depends on grain size to the power -2/n through the β coefficient. Increasing the grain size to 1 cm reduces the melt transit time to 54 kyrs, although a melt fraction of 0.0034 which is harder to reconcile with geophysical estimates of melt content underneath mid-ocean ridges.

A larger melt fraction would be compatible with ²³⁰Th constraints but could not be sustained by melting of an upwelling mantle column. However, these calculations assume a very simple system, i.e. 1-D melt percolation through a uniform network in steady state. They do not give any consideration heterogeneities in the melt distribution larger than the grain-scale. It may be possible to reconcile uranium-series disequilibrium and geophysical observations if the mantle is heterogeneous, with high porosity channels.

5.4. Implications for mantle heterogeneities

High melt fraction dunite conduits have been observed in ophiolites and appear necessary to explain chemical disequilibrium between mid-ocean ridge basalts and the mantle residuum (Dick, 1977; Johnson and Dick, 1992; Kelemen et al., 1992; Quick, 1982; Spiegelman and Kelemen, 2003). Dunite conduits form as a buoyant melt, which is saturated in olivine but under-saturated in orthopyroxene (Ortoleva et al., 1987), reacts with pyroxene-bearing

peridotite, simultaneously dissolving the orthopyroxene and precipitating olivine (Kelemen et al., 1997, 1995a, 1995b). The dissolution of pyroxene is an incongruent melting reaction, i.e. more melt is produced by volume than is removed from the system by the precipitation of olivine (Kelemen et al., 1995b), and increases both melt fraction and permeability. Naturally, the rate of dissolution is enhanced in regions where permeability is increased, which, in turn continues to enhance permeability. Thus, a positive feedback, known as the reactive infiltration instability (RII), is established between the opx dissolution and permeability enhancement. Numerical models (Aharonov et al., 1995; Kelemen et al., 1997; Spiegelman et al., 2001; Spiegelman and Kelemen, 2003) have shown that the RII is capable of producing banded dunite structures similar to those found in nature.

Our results have direct implications for melt transport within these conduits. At the grain-scale, permeability is largely controlled by the local melt distribution, which is determined by local variations in the free surface energy of the system. Free surface energy is an intrinsic property of the system composition, i.e. the mineral phases present and the composition of the melt. Since the compositions of our samples are similar to those of partially molten dunite, it stands to reason that melt transport within these dunite conduits adheres to the power-law relationship between permeability and melt fraction that we constrain here. Due to the RII, the melt fraction within dunite conduits is four times the overall mantle melt content (Spiegelman et al., 2001). Therefore, the permeability of these conduits is about 37 times larger than for a homogeneous mantle. Neglecting melt production by RII, the channels would occupy 25% of the mantle, so that channelization would increase the velocity by approximately a factor of 10, making it easier to preserve ²³⁰Th disequilibrium while verifying the mass balance considerations described in the previous section.

The permeability of dunite conduits may further increase if the difference in surface energy between olivine and opx is sufficient to preferentially partition melt to olivine-rich areas (Watson, 1999), increasing melt content in dunite conduit beyond the product of incongruent melting. Lithological melt partitioning has been proposed to occur in mantle systems where olivine and opx are present. However, experimental evidence for melt partitioning in systems with mineralogies similar to the mantle is lacking. Although more research is needed to establish the extent to which the RII and lithological partitioning modify the permeability structure of the mantle, dunite conduits are good candidates for enhancing overall melt transport within the partially molten region of the mantle beneath mid-ocean ridges.

6. Conclusion

This study is the first to use a 3-D imaging technique on synthetic partially molten peridotites to estimate sample permeability. Visual inspection of the digital microstructures shows that for melt fractions as low as 0.02, interconnected melt channels residing along grain edges are the dominant features of the melt network. For melt fractions greater than 0.05, considerable melt pooling and grain boundary wetting are observed in addition to melt channels. Measured connectivity distributions confirm the increased contribution of grain boundary wetting as melt content increases.

The permeability of our samples was computed numerically for sufficiently large representative subvolumes and ranged from 4×10^{-16} to 2×10^{-13} m² for melt fractions ranging from 0.02 to 0.20. The relationship between permeability and local melt fraction is adequately represented by a power law $k = d^2 \phi^n/C$, with d the grain size (approximately 35 µm in our samples), the exponent $n = 2.6 \pm 0.2$, and the geometric constant $C = 58^{+36}_{-22}$. A first-order calculation, based on mass balance in a 1-D melting column, show that our empirical relation implies a melt fractions of order 1% un-

der mid-ocean ridges with upwelling velocities of order 1 myr⁻¹, leading to transit times through the melting column that are consistent with those constrained by uranium-series analyses. Combined with numerical computation, SXµT has proven to be a useful tool for characterizing the microstructure of partially molten peridotites and computing their material properties. The results of this study place important new constraints on melt transport beneath mid-ocean ridges, where partial melting occurs.

Acknowledgements

We thank the beamline scientists who work at 2-BM of the Advanced Photon Source Xianghui Xiao and Francesco De Carlo for their assistance in conducting the tomography experiments. We thank the personnel at the Visual Software Group, specifically Jean-Luc Garnier, for their technical assistance. We also thank Saswata Heir-Majumder, Harrison Lisabeth, Audrey Ougier-Simonin, and Véronique Le Roux for their insightful discussions. This paper was improved by the thorough and constructive comments and suggestions from editor Yanick Ricard and reviewers Takashi Yoshino, Jörg Renner, and Marc Spiegelman. Marc Spiegelman suggested the analysis of Section 5.2. This work is supported by the National Science Foundation under the grants NSF-EAR1250338, NSF-EAR 0753505, and NSF-OCE 1060878.

Appendix A. Supplementary material

Supplementary material related to this article can be found online at http://dx.doi.org/10.1016/j.epsl.2013.12.003.

References

- Aharonov, E., Whitehead, J.A., Kelemen, P.B., Spiegelman, M., 1995. Channeling instability of upwelling melt in the mantle. J. Geophys. Res. 100, 20433–20450. http://dx.doi.org/10.1029/95JB01307.
- Asimow, P., Hirschmann, M., Ghiorso, M., O'Hara, M., Stolper, E., 1995. The effect of pressure-induced solid-solid phase transitions on decompression melting of the mantle. Geochim. Cosmochim. Acta 59, 4489–4506. http://dx.doi.org/10.1016/0016-7037(95)00252-U.
- Beucher, S., 1992. The watershed transformation applied to image segmentation. Scanning Microsc. 6, 299–314.
- Boyd, F.R., England, J.L., 1960. Apparatus for phase-equilibrium measurements at pressures up to 50 kilobars and temperatures up to 1750 °C. J. Geophys. Res. 65, 741–748. http://dx.doi.org/10.1029/jZ065i002p00741.
- Buades, A., Coll, B., Morel, J., 2005. A non-local algorithm for image denoising. Proc. IEEE Comput. Soc. Conf. Comput. Vis. Pattern Recognit. 2, 60–65. http://dx.doi.org/10.1109/CVPR.2005.38.
- Cheadle, M.J., 1989. Properties of texturally equilibrated two-phase aggregates. PhD Thesis. University of Cambridge.
- Chorin, A.J., 1967. A numerical method for solving incompressible viscous flow problems. J. Comput. Phys. 2, 12–26. http://dx.doi.org/10.1016/0021-9991(67)90037-X.
- Cmíral, M., Fitz, J.D., Faul, U.H., Green, D.H., 1998. A close look at dihedral angles and melt geometry in olivine-basalt aggregates: a TEM study. Contrib. Mineral. Petrol. 130, 336-345.
- Connolly, J.A.D., Schmidt, M.W., Solferino, G., Bagdassarov, N., 2009. Permeability of asthenospheric mantle and melt extraction rates at mid-ocean ridges. Nature 462, 209-212. http://dx.doi.org/10.1038/nature08517.
- Dick, H.J.B., 1977. Evidence of partial melting in the Josephine peridotite. In: Dick, H.J.B. (Ed.), Magma Genesis. Department of Geology and Mineral Industries Bulletin 96, Portland, OR, pp. 63–78.
- Dowd, B.A., Campbell, G.H., Siddons, D.P., Marr, R.B., Nagarkar, V.V., Tipnis, S.V., Axe, L., 1999. Developments in synchrotron X-ray computed microtomography at the National Synchrotron Light Source. Proc. SPIE, 224–236. http://dx.doi.org/10.1117/12.363725.
- Evans, R., Tarits, P., Chave, A., White, A., Heinson, G., Filloux, J., Toh, H., Seama, N., Utada, H., Booker, J., Unsworth, M., 1999. Asymmetric electrical structure in the mantle beneath the east pacific rise at 17°S. Science 286, 752–756. http://dx.doi.org/10.1126/science.286.5440.752.
- Faul, U., Fitz Gerald, J., 1999. Grain misorientations in partially molten olivine aggregates: an electron backscatter diffraction study. Phys. Chem. Miner. 26, 187–197. http://dx.doi.org/10.1007/s002690050176/.
- Fitzgerald, R., 2000. Phase-sensitive X-ray imaging. Phys. Today 53, 23–26. http://dx.doi.org/10.1063/1.1292471.

- Fusseis, F., Schrank, C., Liu, J., Karrech, Llana-Fúnez, S., Xiao, X., Regenauer-Lieb, K., 2012. Pore formation during dehydration of a polycrystalline gypsum sample observed and quantified in a time-series synchrotron X-ray micro-tomography experiment. Solid Earth 3, 71–86. http://dx.doi.org/10.1016/j.epsl.2013.03.052.
- Garapić, G., Faul, U.H., Brisson, E., 2013. High-resolution imaging of the melt distribution in partially molten upper mantle rocks: evidence for wetted two-grain boundaries. Geochem. Geophys. Geosyst. 14, 1–11. http://dx.doi.org/ 10.1002/ggge.20066.
- Gray, W.G., 1975. A derivation of the equations for multi-phase transport. Chem. Eng. Sci. 30, 229–233. http://dx.doi.org/10.1016/0009-2509(75)80010-8.
- Harlow, F.H., Welch, J.E., 1965. Numerical calculation of time-dependent viscous incompressible flow of fluid with free surface. Phys. Fluids 8, 2182–2189. http://dx.doi.org/10.1063/1.1761178.
- Hays, J.F., 1966. Lime-alumina-silica. Carnegie Inst. Washingt. Yearbook 65, 234–239.
 Hier-Majumder, S., Ricard, Y., Bercovici, D., 2006. Role of grain boundaries in magma migration and storage. Earth Planet. Sci. Lett. 248, 735–749. http://dx.doi.org/10.1016/j.epsl.2006.06.015.
- Johannes, W., Bell, P., Mao, H., Boettcher, A., Chopman, D., Hays, J., Newton, R., Seifert, F., 1971. An interlaboratory comparison of piston-cylinder pressure calibration using the albite-breakdown reaction. Contrib. Mineral. Petrol. 32, 24–38. http://dx.doi.org/10.1007/BF00372231.
- Johnson, K., Dick, H.J.B., 1992. Open system melting and temporal and spatial variation of peridotite and basalt at the Atlantis II fracture zone. J. Geophys. Res. 97, 9219–9241. http://dx.doi.org/10.1029/94JB02544.
- Kelemen, P.B., Dick, H.J.B., Quick, J.E., 1992. Formation of harzburgite by pervasive melt/rock reaction in the upper mantle. Nature 358, 635–641. http://dx.doi.org/ 10.1038/358635a0.
- Kelemen, P.B., Shimizu, N., Salters, V.J.M., 1995a. Extraction of mid-ocean-ridge basalt from the upwelling mantle by focused flow of melt in dunite channels. Nature 375, 747–753. http://dx.doi.org/10.1038/375747a0.
- Kelemen, P.B., Whitehead, J.A., Aharonov, E., Jordahl, K.A., 1995b. Experiments on flow focusing in soluble porous media, with applications to melt extraction from the mantle. J. Geophys. Res. 100, 475–496. http://dx.doi.org/10.1029/94JB02544.
- Kelemen, P.B., Hirth, G., Shimizu, N., Spiegelman, M., Dick, H.J., 1997. A review of melt migration processes in the adiabatically upwelling mantle beneath oceanic spreading ridges. Philos. Trans. R. Soc., Math. Phys. Eng. Sci. 355, 283–318. http://dx.doi.org/10.1098/rsta.1997.0010.
- Key, K., Constable, S., Liu, L., Pommier, A., 2013. Electrical image of passive mantle upwelling beneath the northern East Pacific Rise. Nature 495, 499–502. http://dx.doi.org/10.1038/nature11932.
- Lundstrom, C.C., Gill, J., Williams, Q., Perfit, M.R., 1995. Mantle melting and basalt extraction by equilibrium porous flow. Science 270, 1958–1961. http://dx.doi.org/10.1126/science.270.5244.1958.
- Madden, T., 1976. Random networks and mixing laws. Geophysics 41, 1104–1125. http://dx.doi.org/10.1190/1.2035907.
- McKenzie, D., 1984. The generation and compaction of partially molten rock. J. Petrol. 25, 713–765. http://dx.doi.org/10.1093/petrology/25.3.713.
- McKenzie, D., 1985. ²³⁰Th–²³⁸U disequilibrium and the melting process beneath ridge axes. Earth Planet. Sci. Lett. 72, 149–157. http://dx.doi.org/10.1016/0012-821X(85)90001-9.
- McKenzie, D., 2000. Constraints on melt generation and transport from Useries activity ratios. Chem. Geol. 162, 81–94. http://dx.doi.org/10.1016/S0009-2541(99)00126-6.
- Ortoleva, P., Chadam, J., Merino, E., Sen, A., 1987. Geochemical self-organization II: the reactive-infiltration instability. Am. J. Sci. 287, 1008–1040. http://dx.doi.org/10.2475/ajs.287.10.1008.
- Quick, J.E., 1982. The origin and significance of large, tabular dunite bodies in the Trinity Peridotite, Northern California. Contrib. Mineral. Petrol. 78, 413–422. http://dx.doi.org/10.1007/BF00375203.
- Renner, J., Viskupic, K., Hirth, G., Evans, B., 2003. Melt extraction from partially molten peridotites. Geochem. Geophys. Geosyst. 4, 8606. http://dx.doi.org/10.1029/2002GC000369.
- Ribe, N., 1985. The generation and composition of partial melts in the Earth's mantle. Earth Planet. Sci. Lett. 73, 361–376. http://dx.doi.org/10.1016/0012-821X(85)90084-6.
- Ricard, Y., Bercovici, D., Schubert, G., 2001. A two-phase model for compaction and damage: 2. Applications to compaction, deformation, and the role of in-

- terfacial surface tension. J. Geophys. Res. 106, 8907–8924. http://dx.doi.org/
- Ryan, M.P., Blevins, J.Y.K., 1987. The viscosity of synthetic and natural silicate melts and glasses at high temperatures and 1 bar (10⁵ Pascals) pressure and at higher pressures. U.S. Geol. Surv., vol. 1764. US Government Printing Office. http://dx.doi.org/10.1029/88E001059.
- Sims, K.W.W., Goldstein, S.J., Blichert-toft, J., Perfit, M.R., Kelemen, P., Fornari, D.J., Michael, P., Murrell, M.T., Hart, S.R., DePalo, D.J., Layne, G., Ball, L., Jull, M., Bender, J., 2002. Chemical and isotopic constraints on the generation and transport of magma beneath the East Pacific Rise. Geochim. Cosmochim. Acta 66, 3481–3504. http://dx.doi.org/10.1016/S0016-7037(02)00909-2.
- Spiegelman, M., Elliott, T., 1993. Consequences of melt transport for uranium series disequilibrium in young lavas. Earth Planet. Sci. Lett. 118, 1–20. http://dx.doi.org/10.1016/0012-821X(93)90155-3.
- Spiegelman, M., Kelemen, P.B., 2003. Extreme chemical variability as a consequence of channelized melt transport. Geochem. Geophys. Geosyst. 4, 1055–1072. http://dx.doi.org/10.1029/2002GC000336.
- Spiegelman, M., Kelemen, P.B., Aharonov, E., 2001. Causes and consequences of flow organization during melt transport: The reaction infiltration instability in compactible media. J. Geophys. Res. 106, 2061–2077. http://dx.doi.org/ 10.1029/2000|B900240.
- Stolper, E., Walker, D., Hager, B.H., Hays, J.F., 1981. Melt segregation from partially molten source regions: The importance of melt density and source region size. J. Geophys. Res. 86, 6261–6271. http://dx.doi.org/10.1029/JB086iB07p06261.
- Stracke, A., Bourdon, B., McKenzie, D., 2006. Melt extraction in the Earth's mantle: Constraints from U-Th-Pa-Ra studies in oceanic basalts. Earth Planet. Sci. Lett. 244, 97–112. http://dx.doi.org/10.1016/j.epsl.2006.01.057.
- The MELT Seismic Team, 1998. Imaging the deep seismic structure beneath a midocean ridge: the MELT experiment. Science 280, 1215–1218. http://dx.doi.org/10.1126/science.280.5367.1215.
- Toramaru, A., Fujii, N., 1986. Connectivity of melt phase in a partially molten peridotite. J. Geophys. Res. 91, 9239–9252. http://dx.doi.org/10.1029/IB091iB09p09239.
- Vincent, L., 1993. Morphological grayscale reconstruction in image analysis: Applications and efficient algorithms. IEEE Trans. Image Process. 2, 176–201. http://dx.doi.org/10.1109/83.217222.
- Von Bargen, N., Waff, H.S., 1986. Permeabilities, interfacial areas and curvatures of partially molten systems: Results of numerical computations of equilibrium microstructures. J. Geophys. Res. 91, 9261–9276. http://dx.doi.org/10.1029/IB091iB09p09261.
- Wark, D.A., Watson, E.B., 1998. Grain-scale permeabilities of texturally equilibrate, monomineralic rocks. Earth Planet. Sci. Lett. 164, 591–605. http://dx.doi.org/ 10.1016/S0012-821X(98)00252-0.
- Wark, D.A., Williams, C.A., Watson, E.B., Price, J.D., 2003. Reassessment of pore shapes in microstructurally equilibrated rocks, with implications for permeability of the upper mantle. J. Geophys. Res. 108, 2050–2065. http://dx.doi.org/ 10.1029/2001/B001575.
- Watson, E.B., 1999. Lithologic partitioning of fluids and melts. Am. Mineral. 84, 1693–1710.
- Watson, H.C., Roberts, J.J., 2011. Connectivity of core forming melts: Experimental constraints from electrical conductivity and X-ray tomography. Phys. Earth Planet. Inter. 186, 172–182. http://dx.doi.org/10.1016/j.pepi.2011.03.009.
- Weickert, J., Romeny, B.M.T.H., Viergever, M.A., 1998. Efficient and reliable schemes for nonlinear diffusion filtering. IEEE Trans. Image Process. 7, 398–410. http://dx.doi.org/10.1109/83.661190.
- York, D., Evensen, N.M., Martínez, M.L., De Basabe Delgado, J., 2004. Unified equations for the slope, intercept, and standard errors of the best straight line. Am. J. Phys. 72, 367–375.
- Yoshino, T., Yamazaki, D., Mibe, K., 2009. Well-wetted olivine grain boundaries in partially molten peridotite in the asthenosphere. Earth Planet. Sci. Lett. 283, 167–173. http://dx.doi.org/10.1119/1.1632486.
- Zhu, W., Hirth, G., 2003. A network model for permeability in partially molten rocks. Earth Planet. Sci. Lett. 212, 407–416. http://dx.doi.org/10.1016/ S0012-821X(03)00264-4.
- Zhu, W., Gaetani, G.A., Fusseis, F., Montési, L.G.J., De Carlo, F., 2011. Microtomography of partially molten rocks: three-dimensional melt distribution in mantle peridotite. Science 332, 88–91. http://dx.doi.org/10.1126/science.1202221.